Use of a Monte-Carlo based probability matrix for 3D iterative reconstruction of MADPET–II data

Magdalena Rafecas, *Member, IEEE,* Brygida Mosler, Melanie Dietz, Markus Pögl, Alexandros Stamatakis, David P. McElroy, *Member, IEEE,* Sibylle I. Ziegler *Member, IEEE.*

***Abstract*— The small animal PET scanner MADPET-II, currently under development, is characterized by a small diameter (71 mm), two radial layers of detectors and by small LSO crystal elements read out individually by avalanche photodiodes. To exploit this configuration, aimed at achieving high resolution and high sensitivity, we intend to reconstruct a FOV almost as large as the opening of the device. However, parallax errors may hinder this task. To overcome this problem, our objective was to implement fully 3D reconstruction techniques (MLEM and OSEM) based on an accurate description of the system response. The main feature of our method is the calculation of the probability system matrix by means of Monte-Carlo simulations. This approach requires the sorting of the simulated data into the matrix, a computationally expensive procedure hindered by the huge size of the matrix. In order to handle this problem, we have employed a database management system (DB2), which has proven to be a practical solution. In this work we also studied the effect of applying the underlying symmetries within the matrix to reduce statistical noise affecting the matrix elements and to save disk space. The results showed that this procedure increases the SNR and contrast. The transaxial resolution calculated from a phantom consisting of 7 point sources degraded slowly towards the edges of the FOV: for a source at $\mathrm{r} = 0$ the FWHM was 1.0 mm, while for a source at $\mathrm{r} = 30$ mm, the FWHM was 2.0 mm. The use of the symmetries allowed us to reduce the resolution degradation (FWHM $= 1.4$ mm for $\mathrm{r} = 30$ mm). Despite the gaps between modules and between detectors, rotation of the scanner was not needed. For the 3D case, an important issue is to improve the accuracy and the statistical quality of the matrix. This is the objective of our future work.**

***Index Terms*— small animal PET, iterative reconstruction, Monte Carlo simulations, system probability matrix.**

I. Introduction

PET studies of mice and rats need high resolution, high sensitivity scanners. However, these properties usually exclude each other. The new scanner MADPET-II, currently under development [1], has been conceived to fulfill both of these requirements. A small diameter and two radial layers will result in high sensitivity and the use of small crystals will enable us to achieve high spatial resolution [2]. However, the size of the animals compels us to reconstruct a FOV with a diameter almost as large as the diameter of the system. This implies that a large part of the FOV is affected by parallax errors as a consequence of crystal penetration.

Statistical iterative methods may help to reduce the impact of the parallax effect in the image, since they can incorporate a model of the system response. In the absence of noise, the imaging process can be described as $\bar{\mathbf{y}} = \mathbf{A}\,\mathbf{f}$, where $\mathbf{A}$ is the *system probability matrix*, the vector $\mathbf{f}$ corresponds to the voxelized image and $\bar{\mathbf{y}}$ to the measured data. The matrix elements A_{ij} (*probability weights*) are defined as the probability of detecting an annihilation event emitted from image pixel j by a detector pair i. They are usually calculated by computing the intersection of the line–of–response (LOR) defined by a pair of detectors with each pixel [3] [4]. More accurate approaches take into account the position of the voxel relative to the detectors [5] or use analytical models or empirical kernels to compensate for crystal penetration effects [6] [7] [8].

Our approach relies on employing Monte Carlo (MC) simulated data to model the detector response, as suggested for clinical PET by Veklerov *et al.* [9]. Our group has proven that for 2D reconstruction of small animal data, the combination of iterative algorithms with a MC based probability matrix results in an almost constant spatial resolution across the whole FOV, for $R_{\mathrm{FOV}} = 93\% R_{\mathrm{scanner}}$ [10].

Nevertheless, the random processes involved in a MC simulation result in matrix elements that are affected by statistical noise. The impact of noise propagation from the matrix into the image depends on the reconstruction method and on the number of simulated events, as we have shown in [11] for 2D acquisitions of a small animal sector PET tomograph.

The aim of the present study was to calculate the probability matrix of MADPET-II using Monte Carlo simulations and to implement statistical iterative reconstruction algorithms for a fully 3D reconstruction of MADPET-II data. The probability matrix should account for the geometric response of the system and scatter within the detector. When compared to the calculation of 2D weights for the sector tomograph MADPET [11], the execution of this objective was hindered by the following issues:

- 3D Monte Carlo simulations are much less effective than 2D simulations. In the latter, to speed up the computations, pairs of photons were emitted within a plane [10]. However, a realistic description of the behavior of MADPET-II requires isotropic emission of photons in 3D.
- Due to the increased number of possible LORs and image voxels for MADPET-II, the size of the corresponding

This work was supported by the *Deutsche Forschungsgemeinschaft* (DFG Zi 615/2), and *Bund der Freunde der Technischen Universität München* (3 2307).

M. Rafecas, B. Mosler, M. Dietz, D. P. McElroy and S. Ziegler are with the Nuklearmedizin, Klinikum rechts der Isar, Technische Universität München, Ismaninger Str. 22, 81675 München, Germany (e–mail: M:Rafecas@lrz.tum.de).

M. Pögl and A. Stamatakis are with the Institut für Informatik, Technische Universität München, Boltzmannstr. 3, 85748 Garching bei München, Germany.

probability matrix $\mathbf{A}$ will be very large.

Given these constraints, our first objective was to implement fast sorting algorithms to create $\mathbf{A}$ from the simulations. The final goal of this work was to check if the available simulations were sufficient to guarantee good image quality. We considered the role of system symmetries to improve the statistical quality of the matrix.

II. Methods

A. The system: MADPET-II

MADPET-II is a high resolution small animal positron emission tomograph, currently under development [12] [1]. The prototype is based on the individual readout of LSO crystals by monolithic APD matrices. The main geometrical feature of MADPET-II is its dual layer configuration [2]: 1152 crystals will be distributed into 18 modules, each one consisting of two radial layers and 8 axial slices. The inner radius of the scanner is 71 mm, and the size of the crystals is $2 \times 2 \times 6$ mm^3 (front layer) and $2 \times 2 \times 8$ mm^3 (back layer). The spacing between crystals is 0.3 mm.

B. Monte Carlo simulations

The geometry and components of MADPET-II, including non-sensitive materials (APDs, housing, lead shielding, optical coupling, etc.) have been described in Monte Carlo (MC) code [2] by means of *GEANT 3.0* [13]. Positron range and non–collinearity were not included to speed up the computations.

To calculate the probability matrix, a phantom consisting of a radioactive cylinder ($\varnothing = 70$ mm, $L = 18.7$ mm) homogeneously filled with activity was simulated. Neither scattering nor attenuation media within the phantom was considered. Instead of running a unique, long simulation, we preferred to perform sequential, shorter simulations. A total of 1.95×10^{10} events were randomly generated within the cylinder volume and two gamma rays were isotropically emitted in 3D, but those trajectories not intersecting the scanner volume were not tracked. A photon was considered detected if it deposited energy within a single crystal by one or more interactions. In this study, due to the low detection efficiency of 3D simulations, no energy threshold was applied. This implied that photons that were scattered in the non-sensitive materials were also included.

The output of the simulations was a binary list–mode file (`.geant`) including the following information for each recorded event in a structure of 36 bytes: LOR number, energy deposited by each photon, and their emission vertex.

C. Calculation of the probability matrix

We assumed that N_{ij} (number of detected events generated within a certain image voxel j and detected by a certain pair i in the simulations), is proportional to the detection probability A_{ij}. A non–normalized probability matrix $\tilde{\mathbf{A}}$ could be thus calculated by assigning N_{ij} to the element $\tilde{A}_{ij}$. This procedure allows us to keep the accuracy without increasing storage, because the elements of $\tilde{\mathbf{A}}$ are stored as short integers. Normalizing the matrix to have absolute detection probabilities would have implied the storage of A_{ij} as floating or double precision numbers, thus losing accuracy in the first case or increasing storage in the latter.

To determine N_{ij}, we first "voxelized" the FOV. For that purpose we chose a 3D array of $140 \times 140 \times 40$ cubic voxels of size (0.5 mm)^3. During this process, an energy threshold can be applied so that the binary file corresponding to the voxelized data (`.index` file) only contains information about i and j for each detected event (a structure of 8 bytes per event).

The sorting of the voxelized data according to ordered values for j (voxel) and i (LOR) is a computationally expensive procedure because of the range of values taken by i and j: $i \in [0, 1152 \times 1152)$ and $j \in [0, 140 \times 140 \times 40)$. This implies a matrix dimension of 1.04×10^{12} (≈ 11 terabytes). A sorting technique based on increasing by one the elements of a vector stored on the memory, as employed for the 2D case [10], was thus not possible. To overcome this problem, we used the database management system *DB2* from IBM (see next section).

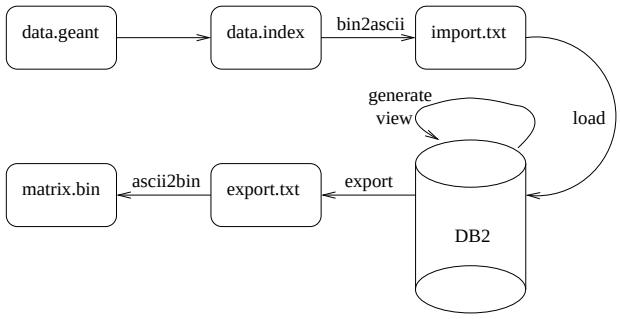

Fig. 1. *Outline of the data process.*

D. The database system

We decided to use DB2 [14] [15] instead of e.g. MySQL [16] since at the time of the implementation DB2 provided the capability to store extremely large individual tables. Currently, the data acquisition process is performed in a pipeline-like fashion as outlined in figure 1. Initially, all `.geant` files are converted into `.index` binary files (see last section II-C) which in turn are transformed into the required plain ASCII input file for DB2. Thereafter, the text files are loaded into the database via a simple `load` operation, where each table entries is of type (i, j, w), with $w = 1$ (i.e., one table entry per simulated event). At this point, the number of table entries is the same as the number of simulated events. The most important step of the data preparation process consists of merging table entries for each (i, j) combination, such that (i, j, w_1) and (i, j, w_2) are merged into $(i, j, w_1 + w_2)$, where the third index is frequency of appearance of each (i, j) combination. This step is carried out by invoking a `view` operation on the database, and once performed, we get N_{ij}, the elements of the matrix. The table can be easily updated if additional simulations are run by loading the new data and invoking a `view` operation

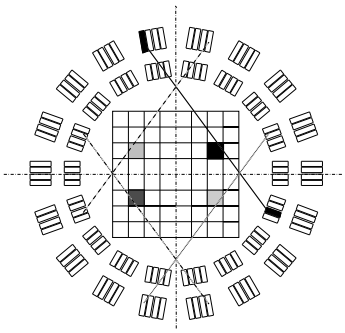

Fig. 2. *Frontal view of MADPET-II (only LSO crystals). The probability weight corresponding to the black pixel and the LOR represented as a solid line is the same as the one corresponding to the dashed line and the top left pixel, the dotted line and the bottom right pixel, and to the dashed–dot–dot line and the bottom left pixel.*

again. This kind of operation can be efficiently performed by database systems such as DB2. Finally, since DB2 does not allow us to export the data in a binary format, the data created by the `view` operation are exported into a plain ASCII text file, which in turn is transformed into a binary file. This `.bin` file contains all non–zero elements of the matrix, storing the triplet (i, j, N_{ij}) as a structure of 12 bytes.

E. Matrix symmetries

The statistical quality of $\tilde{\mathbf{A}}$ can be increased by making use of the symmetries inherent in the MADPET–II matrix (see Fig. 2); these symmetries also allowed us to save disk space. Considering the transaxial plane and a centered grid, the value related to the weight corresponding to voxel j (black square) and LOR i (solid line) is the same as for $A_{\hat{i}\hat{j}}$, $\hat{i}$ and $\hat{j}$ being the values of the LOR and the pixel after reflections about the axes. In addition to this, we can find four more identical values after reflection about the OXY plane.

By using these symmetries, we calculated $\tilde{A}_{ij}^{\text{sym}}$ as the sum over all coincidences $N_{\hat{i}\hat{j}}$ for all pairs $(\hat{i}, \hat{j})$ related to (i, j). Since the matrix elements corresponding to the eight pairs $(\hat{i}, \hat{j})$ should be equal, it was sufficient to store $\tilde{A}_{ij}^{\text{sym}}$.

F. Characterization of the probability matrix

The accuracy of the probability matrix is determined by the number of simulated events. A high number of simulated coincidences is thus desirable to reduce the noise in $\tilde{\mathbf{A}}$, however, it is difficult to know *a priori* if the simulated data allow an accurate description of the system response or if further simulations are needed.

To estimate the accuracy of the probability matrix, we determined the number of non–zero matrix elements, $N^{\text{non–zero}}$, and the "mean relative error", defined as:

$$\bar{\sigma}_{\text{rel}} \equiv \frac{\sum_{i=0;j=0}^{I-1;J-1} \frac{\sigma_{\tilde{A}_{ij}}}{\tilde{A}_{ij}}}{N^{\text{non–zero}}}, \tag{1}$$

where $\sigma_{\tilde{A}_{ij}}$ is the standard deviation relative to $\tilde{A}_{ij}$. (Assuming that the emission and detection of photons are Poisson processes, we can write: $\sigma_{\tilde{A}_{ij}} = \sqrt{N_{ij}}$.) The motivation for using $\sigma_{\tilde{A}_{ij}} = \sqrt{N_{ij}}$ is the following: Ideally, if we had described the true probability matrix, new simulations would not imply an increase of the number of non–zero elements, but rather a decrease of $\bar{\sigma}_{\text{rel}}$. We can expect that every time we update the matrix by processing new simulated data, $\bar{\sigma}_{\text{rel}}$ will diminish, as we have seen for the 2D case [11], unless the values of $\tilde{\mathbf{A}}$ would have converged towards the true values. Hence, the "evolution" of $\bar{\sigma}_{\text{rel}}$ is related to the accuracy of $\tilde{\mathbf{A}}$.

G. Reconstruction techniques

We implemented the reconstruction algorithm MLEM [17] and its accelerated version OSEM [18], since OSEM proved to be a very robust technique, even when using probability matrices generated from noisy simulations [11].

The input data were arranged in list–mode histograms, i.e., the total number of counts detected by every pair of channels ordered according to the LOR index. Since no sinograms are used and the indexing of the LORs is not related to the corresponding projection geometry, the subsets were arranged according to a random distribution of the LORs. The dimensions of the reconstructed 3D FOV were $R = 35$ mm and $L = 18$ mm. For a better understanding of the impact of statistical noise from the simulations on the image, no smoothing was performed.

H. Simulated phantoms

To study image quality, a centered radioactive cylinder ($R = 25$ mm, $L = 18.7$) was simulated. Neither scattering nor attenuation media within the phantom were considered. Within the cylinder, two rods ($R = 6$ mm) with different activity were placed at ± 12 mm from the center. One of the rods contained no activity ("cold"), while the concentration within the rest of the disc (background) was 0.3 times lower than within the active rod ("hot"). The number of detected coincidences originating within the phantom was 7.5×10^6.

To study the impact of crystal penetration on the resolution, a phantom consisting of 7 point sources located at intervals of 5 mm at $z = 0$ was simulated (5.1×10^6 detected coincidences). The location of the first source corresponds to the center of the scanner, and the plane containing the sources lies between the two central rings of detectors, thus not directly faced by any one ring.

I. Figures–of–merit

Three different regions–of–interest (ROI) were considered when dealing with transaxial images of the first simulated phantom: two circular ROIs ($R = 5$ mm), corresponding to the active and non–active rods, and the cylinder without rod inserts. The image quality was quantified by means of the following figures–of–merit:

- *Signal–to–noise ratio (SNR)*: For the "cold" and "hot" ROIs we calculated: $SNR_{\text{ROI}} \equiv |\mu_{\text{ROI}} - \mu_{\text{cyl}}|/\sigma_{\text{cyl}}$, with

μ_{ROI} being the average concentration within the chosen ROI, and μ_{cyl} the average concentration within the disc (without rods); σ_{cyl} is the standard deviation of the active background. Ideally, μ_{cold} is 0.

- *Contrast*: For a certain ROI related to the active disc, the contrast was defined as: $C_{\text{ROI}} \equiv |\mu_{\text{ROI}} - \mu_{\text{cyl}}|/\mu_{\text{cyl}}$. (Ideal values: $C_{\text{cold}} = 1$ and $C_{\text{hot}} = 2.3$).
- *Mispositioned events*: The ratio of events within the cold rod relative to the total number of counts within the image was calculated.
- *Spatial resolution*: The FWHM of the radial and tangential profiles of the point sources was determined by interpolation.

III. Results

A. Database performance

In Table I we briefly summarize the execution times for loading and adding experimental data to the database. The first two rows correspond to the process of converting two binary `.index` files of 131 MB and 349 MB into ASCII format. The 131–MB `.index` file was loaded into a table, and this table was updated using the data from the 349–MB `.index` file. The updated table was exported as an ASCII file. For comparison purposes, in Table I we also show the processing time required to export the table related to the 131–MB `.index` file. Finally, these data were converted into binary files by executing `ascii2bin`. The column on the far left shows, for reference, the size of the related input `.index` files, and the column right–most shows the size required by the files obtained after the operation described in the second column. The disk space required to store the files in the database (383 MB for the 131–MB file, 1020 MB for the 349–MB file, and 1403 MB for the table obtained after loading both files), is related to the tables before merging those entries sharing identical values of i and j. For all cases, additional 29 MB were required by the database for internal management.

All these operations were carried out with an AMD Athlon processor, 900 MHz. It can be seen that the size of the exported ASCII data are inferior to the size of the imported ASCII data due to the merging operation described in Section II-D. The size of the output binary file (the matrix) is larger than the size of the corresponding `.index` files. This is due to two facts: On one hand, for this example, not many pairs (i, j) were found more than once; on the other hand, each simulated event was represented in the input file as an 8–byte structure, while every element of the matrix file corresponds to a 12–byte structure.

B. Characteristics of the system matrices

A total of 2.22×10^8 detected coincidences were sorted to create the system matrix. For $\tilde{\mathbf{A}}$, this represented a mean of 374 detected events per voxel (considering only those voxels in which a detected coincidence originated), and a mean of 890 detected events per LOR (considering only those LORs having detected at least one coincidence). The use of symmetries implied an increase of the statistical quality of the matrix, $\tilde{\mathbf{A}}^{\text{sym}}$, which related to an average of 2994 coincidences per voxel, and 7118 coincidences per LOR.

TABLE I

Database performance.

Input data size	Command	Time (min:secs)	File size
131 MB	bin2ascii	0:22	238 MB
349 MB	bin2ascii	1:12	635 MB
131 MB	load	5:12	383 MB
349 MB	load	13:03	1020 MB
349 MB to 131 MB	add data	17:12	1403 MB
131 MB	export	10:12	213 MB
480 MB	export	46:55	612 MB
131 MB	ascii2bin	0:43	175 MB
480 MB	ascii2bin	2:07	504 MB

For $\tilde{\mathbf{A}}$, while the maximum number of detected events per LOR and per voxel, $N^{\max}$, was found to be 21, the average $\bar{N}$, calculated over the number of non–zero matrix elements, was 1.37, as a consequence of the fact that about 76% of the non–zero matrix elements were related to only one detected pair of photons per LOR and per voxel, i.e., $N_{ij} = 1$.

For $\tilde{\mathbf{A}}^{\text{sym}}$, the values obtained for $\bar{N}$ and $N^{\max}$ were 2.2, and 41, respectively. The number of matrix elements related to $N_{ij} = 1$ was reduced to 61%.

About 76% of the total number of voxels were represented in $\tilde{\mathbf{A}}$, and the number of LORs having detected at least one event was 249,938. These values increased slightly for $\tilde{\mathbf{A}}^{\text{sym}}$, the matrix calculated using the symmetries.

Table II shows the main properties of the system matrices (with and without symmetries). The disk space corresponds to the matrix stored as a binary file. It can be seen, as expected, that the statistical quality of the matrix was improved when using symmetries: the mean relative error, $\bar{\sigma}_{\text{rel}}$, decreased from 91.6% to 82.6% and whereas the number of non–zero elements[1] increased by a factor of 5, the disk space required was 0.63 times smaller.

TABLE II

Properties of the calculated probability matrices.

Sym.	$N_{\text{non–zero}}$	$\bar{\sigma}_{\text{rel}}$	disk space (DB2 table)	disk space (binary)
no	1.62×10^8	91.6%	3.6 GB	1.9 GB
yes	8.07×10^8	82.6%	2.2 GB	1.2 GB

In table II it can be seen that the space required to store the matrix as a table in the database is larger that the size obtained after exporting the table values and posterior conversion into a binary file. In both cases, the space required for the database was ≈ 1.8 times larger that for the binary files. To save disk space, the tables can be removed. If required, values of the matrix as a binary file can be reloaded into a new table. For $\tilde{\mathbf{A}}^{\text{sym}}$, this process took 39 minutes, and for $\tilde{\mathbf{A}}$, 67 minutes.

[1]For comparison purposes, the number of non–zero weights for $\tilde{\mathbf{A}}^{\text{sym}}$ was multiplied by the number of symmetries to get the same size as for $\tilde{\mathbf{A}}$.

C. Image quality

As will be shown in the following subsections, the use of $\tilde{\mathbf{A}}^{\text{sym}}$ instead of $\tilde{\mathbf{A}}$ slightly improved SNR and contrast. However, when using OSEM, the reconstruction process was slowed by the fact that, for each non–zero element of $\tilde{\mathbf{A}}^{\text{sym}}$, the corresponding eight "symmetric" elements could belong to different subsets.

The random grouping of the LORs for OSEM reconstruction proved to be adequate. For N iterations and S subsets, the reconstructed images were almost identical as those obtained using MLEM and $N \times S$ iterations. For this reason, only MLEM images are shown in this paper.

1) SNR, contrast and mispositioned events: In figure 3 the reconstructed data from the simulated cylindrical phantom with two rod inserts are shown (MLEM, 60 iterations). The image on the left corresponds to the use of $\tilde{\mathbf{A}}$ for the reconstruction, while the image on the right was reconstructed after applying the symmetries of the matrix to improve its statistical quality ($\tilde{\mathbf{A}}_{\text{sym}}$). In both cases, the images in figure 3 as well as the the values in table III were obtained after adding all the transaxial planes. It can be seen that using $\tilde{\mathbf{A}}_{\text{sym}}$ resulted in a less noisy image (see also table III).

TABLE III

SNR AND CONTRAST FOR A SIMULATED CYLINDRICAL PHANTOM WITH TWO ROD INSERTS RECONSTRUCTED BY MEANS OF MLEM AND 60 ITERATIONS.

Sym.	SNR_{hot}	SNR_{cold}	C_{hot}	C_{cold}	Mispos. evts.
no	6.7	2.5	2.1	0.8	0.80%
yes	7.2	2.7	2.3	0.8	0.64%

In figure 4, the values of SNR and contrast are plotted as a function of the axial plane. It can be observed that when using $\tilde{\mathbf{A}}_{\text{sym}}$, contrast and SNR were increased. The improvement of SNR was particularly large for the active rod, in agreement with the results presented in [11]. While the contrast remained almost constant over the whole axial FOV, the values for SNR fluctuated. In both cases, for the extern slices ($|dz| > 8$ mm) SNR and contrast worsened. The obtained values for the contrast were less than the ideal ones, but this difference was reduced when $\tilde{\mathbf{A}}_{\text{sym}}$ was utilized.

The mispositioning within the cold rod as a function of the axial plane can be seen in figure 5. The observed trend is similar to the one observed for the SNR: more accurate values when

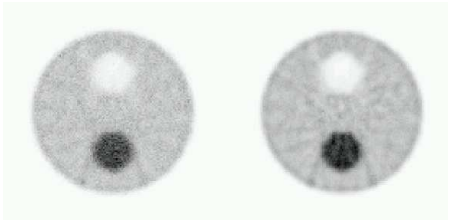

Fig. 3. *Transaxial view of a simulated phantom reconstructed by means of MLEM (60 iterations). Left: reconstruction using $\tilde{\mathbf{A}}$. Right: reconstruction using $\tilde{\mathbf{A}}^{sym}$.*

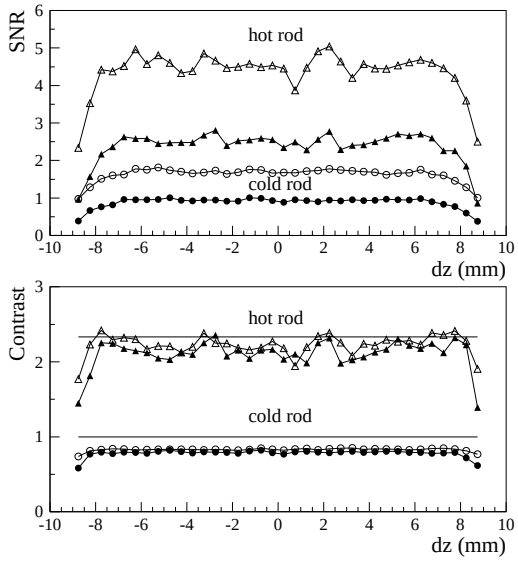

Fig. 4. *Signal–to–noise ratio and contrast for the active (triangles) and non–active (circles) rods related to the cylinder background reconstructed by means of MLEM (60 iterations). The filled symbols correspond to the use of $\tilde{\mathbf{A}}$, while the open ones refer to $\tilde{\mathbf{A}}_{sym}$. The horizontal lines in the lower plot represent the ideal values for C_{hot} and C_{cold}.*

using $\tilde{\mathbf{A}}_{\text{sym}}$, and a worsening towards the axial edges of the FOV.

2) Spatial resolution: The reconstructed point sources using $\tilde{\mathbf{A}}$ (thick line) and $\tilde{\mathbf{A}}_{\text{sym}}$ (thin line) are shown in figure 6. The corresponding FWHM of these profiles is depicted in figure 7 (bottom). The plot at the top represents the FWHM for the tangential profiles of each source. Since the sources were located within a plane at $z = 0$ (gap between the two central rings of detectors), the two central reconstructed planes ($z = \pm 0.5$ mm) were added. For comparison, the FWHM obtained when using FBP (applied to dedicated simulations for

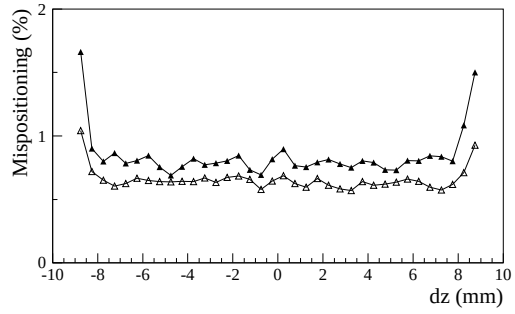

Fig. 5. *Percentage of mispositioned events within the cold rod. The filled symbols correspond to using $\tilde{\mathbf{A}}$, while the open ones refer to $\tilde{\mathbf{A}}_{sym}$.*

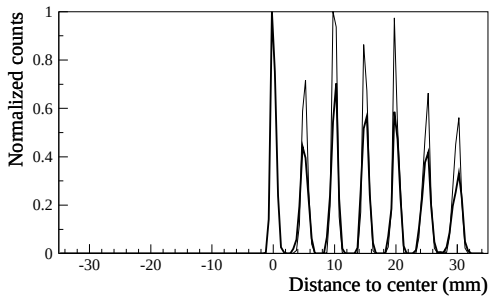

Fig. 6. *Radial profile of a phantom consisting of seven point sources (5 mm spacing), located at $z = 0$. The thick line corresponds to using $\tilde{\mathbf{A}}$, while the thin line is related to $\tilde{\mathbf{A}}_{sym}$.*

every source position with rotation of the scanner in 20 steps[2]) are also plotted.

The variations in the system response as a function of the radial position (see figure 6) might be a consequence of the inaccuracy of the probability matrix, which does not compensate correctly for the non–homogeneous sensitivity across the transaxial FOV. The system response was more homogeneous regarding the source position after enhancing the statistics of the matrix ($\tilde{\mathbf{A}}_{\text{sym}}$).

MLEM combined with a Monte–Carlo based probability matrix proved to reduce the impact of crystal penetration in the resolution: the FWHM degraded slowly, from 1.0 mm at the center to 2.0 mm at $r = 30$ mm (average over the tangential and the radial values). The use of $\tilde{\mathbf{A}}_{\text{sym}}$ instead of $\tilde{\mathbf{A}}$ improved the spatial resolution (except at the center, due to the presence of some artifacts). For a source at $r = 30$ mm, the FWHM was 1.4 mm at 30 mm. When compared to the results obtained by means of FBP and 20 rotation steps, (symbol $(*)$ in graphs of figure 6), we can observe that our approach reduces the degradation of resolution resulting from crystal penetration.

IV. Discussion & Conclusions

For iterative reconstruction, the system response (geometrical efficiency, crystal penetration, etc.) needs to be modeled appropriately. The corresponding matrix is object–independent, since it only depends on the characteristics of the tomograph. Our approach proposes the off–line computation of the related matrix by means of Monte–Carlo simulations.

The issue of scatter and attenuation has not been addressed in this work. These effects could be compensated by including an additional matrix in the reconstruction algorithm [20]. An alternative technique could be to run dedicated MC simulations of every object under study, assuming that the attenuation properties of the object under study are known. This method, developed for SPECT, models attenuation and scatter into the probability matrix (see [21]).

The present study shows that fully 3D statistical image reconstruction using a Monte–Carlo based system probability

[2]The FBP data belong to the work described in [19].

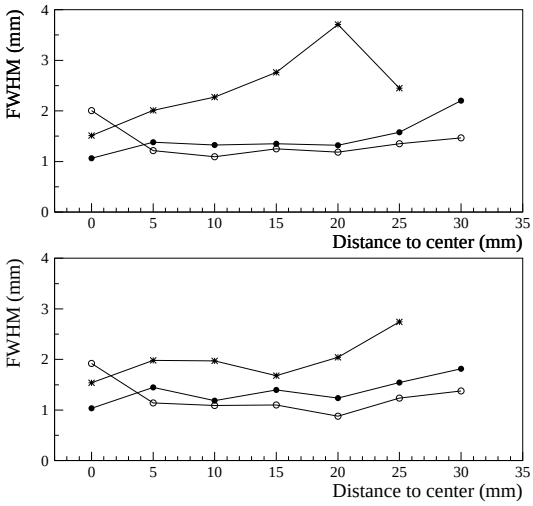

Fig. 7. *Tangential (top) and radial (bottom) resolution across the FOV obtained from the profiles of a phantom consisting of seven point sources (5 mm spacing). The data were reconstructed by means of MLEM (60 iterations) and $\tilde{\mathbf{A}}$ (•) and $\tilde{\mathbf{A}}_{sym}$ (○). For comparison, data from simulated point sources at different positions were reconstructed by means of FBP (see [19]) are also plotted ($*$).*

matrix is feasible. The database management system proved to a very practical framework to handle, sort, store and access the large amounts of data related to the MC simulations and to the probability matrix in an efficient manner. Furthermore, the deployment of a database scheme facilitated the addition of supplementary MC simulation data.

Our approach allowed us to reconstruct a larger FOV without compromising the resolution, despite the high statistical noise affecting the probability matrix. We have seen that a small reduction of statistical noise within the matrix, achieved by applying the matrix symmetries, improved SNR, contrast and spatial resolution. From these results, and from our study of the 2D case [11], we can thus expect that image quality could be further improved if less noisy, more accurate matrices were used.

For that purpose, in addition to performing new simulations, different strategies have been considered for future work, such as applying symmetry considerations directly to the simulated data, instead of to the probability matrix: since the exact emission vertex of each coincidence is known, for each detected event we can generate 36×2 new events by considering the 36 symmetry axes of the scanner, and its symmetry regarding the OXY–plane. This approach, however, implies the increase of the size of the simulated data by a factor of 72. To avoid the storage of the new "symmetrical" events, we have implemented a procedure that allows direct access to the database tables during the calculation of the "symmetrical" coincidences. This routine also allows us to to sort the events from the `.geant` file directly into a database table. Another objective of our group is to investigate the feasibility of accessing the elements of the

database tables during the reconstruction process. This step also comprises the optimization of database performance.

ACKNOWLEDGMENT

The authors would like to thank Dr. Irène Buvat at U494 INSEREM, CHU Pitié–Salpêtrière, Paris, France, for helpful discussions, and Dr. Mary Spilker of the Nuklearmedizinische Klinik, TU M¨unchen, M¨unchen, Germany, for her review of the manuscript.

REFERENCES

[1] D. P. McElroy, W. Pimpl, M. Djelassi, B. J. Pichler, M. Rafecas, T. Schüler, and S. I. Ziegler, "First results from MADPET–II: A novel detector and readout system for high resolution PET," in *IEEE NSS MIC Conf. Rec.*, 2003.

[2] M. Rafecas, G. Böning, B. J. Pichler, E. Lorenz, M. Schwaiger, and S. I. Ziegler, "A Monte Carlo study of high resolution PET with granulated dual layer detectors," *IEEE Trans. Nucl. Sci.*, pp. 1490–1495, 2001.

[3] G. T. Gullberg, R. H. Huesman, J. A. Malko, N. J. Pelc, and T. F. Budinger, "An attenuated projector–backprojector for iterative SPECT reconstruction," *Phys. Med. Biol.*, pp. 799–816, 1985.

[4] G. T. Herman and L. B. Meyer, "Algebraic reconstruction techniques can be made computationally effi cient," *IEEE Trans. Med. Imag.*, pp. 600–609, 1993.

[5] A. Terstegge, S. Weber, H. Herzog, and H. W. M. und H. Halling, "Resolution and better quantifi cation by tube of response modelling in 3D PET reconstruction," in *IEEE Nuclear Science Symposium*, 1996, pp. 1603–1607.

[6] V. Selivanov, Y. Picard, J. Cadorette, S. Rodrigue, and R. Lecomte, "Detector response models for statistical iterative image reconstruction in high resolution PET," *IEEE Trans. Nucl. Sci.*, pp. 1168–1175, 2000.

[7] T. Frese, N. C. Rouze, C. A. Bouman, K. Sauer, and G. D. Hutschins, "Quantitative comparision of FPB, EM and bayesian reconstruction algorithms for the IndyPET scanner," *Trans. Med. Imag.*, pp. 258–276, 2003.

[8] D. Strul, R. B. Slates, M. Dahlbom, S. R. Cherry, and P. K. Marsden, "An improved analytical detector response function model for multilayer small–diameter PET scanners," *Phys. Med. Biol.*, pp. 979–994, 2003.

[9] E. Veklerov, J. Llacer, and E. J. Hoffman, "MLE reconstruction of a brain phantom using a Monte Carlo transition matrix and a statistical stopping rule," *IEEE Trans. Nucl. Sci.*, pp. 603–607, 1988.

[10] G. Böning, B. J. Pichler, M. Rafecas, E. Lorenz, M. Schwaiger, and S. I. Ziegler, "Implementation of Monte Carlo coincident aperture functions in image generation of a high resolution animal positron tomograph," *IEEE Trans. Nucl. Sci.*, pp. 805–810, 2001.

[11] M. Rafecas, G. Böning, B. J. Pichler, E. Lorenz, M. Schwaiger, and S. I. Ziegler, "Effect of noise in the probability matrix used for statistical reconstruction of PET data," *IEEE Trans. Nucl. Sci.*, (in press).

[12] B. J. Pichler, G. Böning, M. Rafecas, W. Pimpl, M. Schwaiger, and S. I. Ziegler, "A 32-channel LSO matrix coupled to a monolithic 4×8 APD array for high resolution PET," *IEEE Trans. Nucl. Sci.*, pp. 1391–1396, 2001.

[13] *GEANT and detector description and simulation tool. Geant's users guide. CERN programm library long writeup W5013*, Application software group (Computing and network division), CERN, Geneva and Switzerland, 1993.

[14] D. Chamberlain, *A complete guide to DB2 universal database.* San Francisco (CA), USA: Morgan Kaufman Publishers, 1998.

[15] B. Schiefer and G. Valentin, "DB2 universal database performance tuning," *Data Engineering Bulletin*, pp. 12–19, 1999.

[16] "MySQL download site," visited 12.11.03. `www.mysql.com`.

[17] L. A. Shepp and Y. Vardi, "Maximum likelihood reconstruction for emission tomography," *IEEE Trans. Med. Imag.*, pp. 113–122, 1982.

[18] H. M. Hudson and R. S. Larkin, "Accelerated image reconstruction using ordered subsets of projection data," *IEEE Trans. Med. Imag.*, pp. 601–609, 1994.

[19] M. Rafecas, G. Böning, B. J. Pichler, E. Lorenz, M. Schwaiger, and S. I. Ziegler, "Inter–crystal scatter in a dual layer, high resolution LSO–APD positron emission tomograph," *Phys. Med. Biol.*, pp. 821–848, 2003.

[20] R. M. Leahy and J. Qi, "Statistical approaches in quantitative positron emission tomography," *Statisticas and Computing*, pp. 147–165, 2000.

[21] D. Lazaro, V. Breton, and I. Buvat, "Feasibility and value of fully of 3D Monte Carlo reconstruction in single photon emission computed tomography," *Nucl Inst Meth*, 2003 (in press).